The final publication is available at

http://doi.org/10.1016/j.ijhydene.2018.03.060

Additional Information

Chemical stability in H$_2$S and creep characterization of the mixed protonic conductor Nd$_{5.5}$WO$_{11.25-\delta}$

S. Escolástico[1,2], V. Stournari[3], J. Malzbender[3], K. Haas-Santo[2], R. Dittmeyer[2], J.M. Serra[1,*]

[1]Instituto de Tecnología Química (Universitat Politècnica de València – Consejo Superior de Investigaciones Científicas), Av. Los naranjos s/n, E-46022, Valencia, Spain
[2]Institute for Micro Process Engineering, Karlsruhe Institute of Technology, Hermann-von-Helmholtz-Platz 1, 76344, Eggenstein-Leopoldshafen, Germany
[3]Institute of Energy and Climate Research, IEK-2, Forschungszentrum Jülich GmbH, D-52425 Jülich, Germany

Abstract

The integration of hydrogen permeable membranes in catalytic membrane reactors for thermodynamically limited reactions such as steam methane reforming can improve the per-pass yield and simultaneously produce a high-purity H$_2$ stream. Mixed protonic-electronic materials based membranes are potential candidates for these applications due to their elevated temperature operation, good stability and potentially low cost. However, a specific mechanical behavior and stability under harsh atmospheres is needed to guarantee sufficient lifetime in real-world processes. This work presents the mechanical characterization and a study of the chemical stability under H$_2$S containing atmospheres for the compound Nd$_{5.5}$WO$_{11.25-\delta}$. Mechanical characterization was performed by micro-indentation and creep measurements in air. Chemical stability was evaluated by XRD and SEM and the effect of the H$_2$S on the transport properties was evaluated by impedance spectroscopy. Under H$_2$S atmospheres, the total conductivity increases at 600 °C and 700 °C. The conductivity increase is attributed to the incorporation of S^{2-} ions in oxide-ion sublattice.

Keywords: lanthanide tungstate, proton-conducting oxide, hydrogen-permeable membrane, H$_2$S stability, mechanical properties

1. Introduction

Currently H$_2$ is mainly produced by steam reforming (SR) of natural gas [1]. H$_2$ is subsequently separated from the reformer and/or water-gas shift reaction co-products and some other compounds present in the gas stream such as CO, CO$_2$, N$_2$, H$_2$S, NH$_3$, and H$_2$O. The need of separation and purification units, usually a pressure swing adsorption step, leads to high specific costs and lowers the energy efficiency. In addition to the separation steps, steam reforming is a thermodynamically-limited process [2, 3].

In this context, the integration of a permselective membrane into a catalytic reactor resulting in a catalytic membrane reactor (CMR) enables the combination of separation and reaction in a single stage, possibly leading to higher product yield and energy efficiency. In the case of steam reforming, the integration of a H$_2$-permeable membrane and a catalyst in the same unit can circumvent both: the

1

separation issue and the thermodynamic limitations imposed on the reactant conversion [2, 4]. In addition to steam reforming, H_2 separation membranes can also be applied for non-oxidative olefin and aromatics production [5] and the water gas shift reaction (WGSR), with the advantage of obtaining an ultra-pure H_2 stream and an increase of the reaction yield by shifting the equilibrium [6, 7].

Among the different H_2 separation membranes, mixed protonic-electronic conductors (MPEC) in addition to palladium alloy membranes [4, 8] appear to be appropriate candidates for this kind of reactions due to their ability to operate at high temperature (>500 °C) and high pressure [9]. Furthermore, they are exceptionally selective to H_2 and present good chemical stability at high temperature (up to 1000 °C) [10]. These materials transport protons through their crystal structure driven by the chemical potential gradient across the membrane. The protons are charge-compensated by transport of electrons or/and oxygen ions without necessity of supplying an external electrical current.

In recent years, mixed proton-electronic-conducting compounds have been extensively studied. The most studied materials are perovskite oxides based on acceptor-doped $BaCeO_3$ and $BaZrO_3$ that present high proton conductivity [11]. However, $BaCeO_3$-based compounds decompose under CO_2 or sulfur-containing atmospheres [12]. On the other hand, $BaZrO_3$-based compounds exhibit a rather high grain boundary resistance that decreases the total conductivity and, in addition, membrane manufacture entails very high sintering temperatures that lead to barium evaporation and a subsequent loss of its properties [13, 14]. Despite these problems, promising H_2 flows have been obtained using doped perovskite membranes [15-18]. Stability and sintering issues have been partially circumvented by the development of mixed solid solutions of $BaCeO_3$ and $BaZrO_3$ [13, 19-22] although electronic conductivity is still limiting the H_2 flux. In the last years, lanthanide tungstates ($Ln_{6-x}WO_{12-y}$) have been widely studied since they present appropriate CO_2 stability [23-25] and electronic conduction that allowed a significant H_2 flux to be reached. Finally, dual phase composite membranes, which consist of an electronic conductor and a protonic conductor [26-29], have shown the highest H_2 flows for proton-electron-conducting ceramic membranes.

The performance of different MPEC based membranes for the water gas shift reaction at high temperature (700-900 °C) has been evaluated, yielding promising results [30, 31]. Recently, methane steam reforming has been accomplished using a $BaZr_{0.7}Ce_{0.2}Y_{0.1}O_{2.9}$ based electrochemical reactor, obtaining an important improvement of the H_2 yield [32]. Non-oxidative methane dehydrogenation (MDA) has also been accomplished using $La_{5.5}W_{0.6}Mo_{0.4}O_{11.25-\delta}$ [33] that was previously realized using a $SrCe_{0.95}Yb_{0.05}O_{3-\delta}$ membrane [34]. In both cases, Mo/H-ZSM5 was used as catalyst. Furthermore, MDA was recently performed by using a tubular membrane made of $BaZr_{0.7}Ce_{0.2}Y_{0.1}O_{3-\delta}$ (BZCY72) and Mo/MCM-22 zeolite as catalyst giving rise to high aromatic yields and improved catalyst stability due to the H^+/O^{-2} co-ionic transport in the membrane [5].

2

In the abovementioned applications, H_2 permeable membranes should work at high temperatures (>500 ºC) and pressures (20-50 bars) under reducing conditions, and usually under atmospheres containing CO_2, CO, H_2O and H_2S [35]. For this reason, mixed proton and electron-conducting compounds need high mechanical and chemical stability under those operation conditions together with high mixed electronic-protonic conductivity to reach high H_2 permeation flux. The chemical stability under H_2S containing atmospheres of different lanthanide tungstates and $BaCeO_3$-$BaZrO_3$ based compounds has been reported. Li et al. concluded that $BaCe_{0.85}Y_{0.15}O_3$ was not stable after a treatment under 5000 ppm H_2S in H_2 at 650 ºC whereas $BaZr_{0.85}Y_{0.15}O_3$ maintained its integrity. Impedance spectroscopy of $BaZr_{0.85}Y_{0.15}O_3$ measured from 450 to 650 ºC under 5000 ppm H_2S balanced with H_2 resulted in lower conductivity than the obtained in free H_2S conditions [36]. Medvedev et al. [37] studied the stability of $BaCe_{0.8-x}Zr_xY_{0.2}O_{3-\delta}$ (0.3<x<0.8) materials under 10% H_2S/Ar at 700 ºC for 10 hours. Compounds with x>0.3 were chemically stable and retained their structure after the treatment. In particular, the total conductivity in dry air of the $BaCe_{0.5}Zr_{0.3}Y_{0.2}O_{3-\delta}$ sample previously treated in H_2S was higher at low temperature than the obtained with the fresh sample. An increase of the conductivity under 0.25-1%H_2S and 90% H_2O in Ar was reported for the electrolyte made of $BaZr_{0.7}Ce_{0.2}Y_{0.1}O_{3-\delta}$ at 850ºC [38]. Stability of NWO and partially-substituted NWO-based compounds has been also proven in different conditions: (a) an atmosphere composed of humidified 10% CO_2 and 90% CH_4 at 800 ºC and 72 hours and (b) a stream comprising 115 ppm H_2S, 4.43% CO_2, 2.12% CO and 92.09% H_2 at 500 ºC and 30 bars for 40 h [23, 25]. Under these conditions $BaCe_{0.9}Eu_{0.1}O_{3-\delta}$ totally decomposed to form barium carbonates and cerium-rich sulfates [18, 23]. In addition, stability of the $La_{5.5}WO_{11.25-\delta}$ (LWO) dense samples has been confirmed at 600 and 900 ºC under syngas conditions containing different contaminants such as HCl, KCl, KOH, NaOH, NaCl [39]. Recently, the stability of an asymmetric membrane made of LWO and MgO as porous support was demonstrated under the atmospheres found in the inlet and the outlet of a WGS-membrane reactor for 96 h at 900 ºC (15% H_2, 34% CO and 51% H_2, reactor inlet and 90% CO_2, 9.9 H_2O and 0.1% H_2 for the reactor outlet) [40].

Despite the stability of lanthanide tungstates under harsh conditions, previous studies have reported that the single phase obtention of the $La_{6-x}WO_{12-y}$ (with y = 1.5x + δ) occurs within a narrow La/W range and out of this region secondary phases as La_2O_3 and $La_6W_2O_{15}$ appear [41, 42]. The reaction of rare earth oxides with H_2S is thermodynamically favoured and they have been studied as desulfurization sorbents at medium and high temperature [43-45]. Subsequently, formation of Nd_2O_3 could occur in the membrane fabrication process giving rise to the Nd_2O_2S formation under H_2S atmospheres that may cause a loss of the electrochemical and structural properties of the material.

In addition, the mechanical properties of these membranes is also an issue for their application. Several studies have been published about the mechanical properties of ceramic membranes focusing mainly on oxygen permeable membranes [46-51]. Regarding proton conducting materials, $La_{5.4}WO_{11.1-\delta}$ (LWO54) mechanical properties were recently reported [52-54].

The current work presents the mechanical characterization and the study of the chemical stability under H_2S containing atmospheres of the mixed proton and electron-conducting compound $Nd_{5.5}WO_{11.25-\delta}$ (NWO). This material was selected due to the important ambipolar conductivity and H_2 permeation flux that NWO-based membranes presents [23, 25, 55, 56], e.g. flux values up to 1.29 mL·min·cm^{-2} were reached at 975 °C by using a hollow fiber membrane with a 170 μm dense layer made of $Nd_{5.5}W_{0.5}Mo_{0.5}O_{11.25-\delta}$ [57].

Mechanical characterization of NWO was performed by means of room temperature micro-indentation and creep measurements in air from 900 °C to 1350 °C. Chemical stability under H_2S containing atmospheres was evaluated by X-ray diffraction and SEM, and the effect of the H_2S on the transport properties of the material was evaluated by electrochemical impedance spectroscopy.

2. Experimental

$Nd_{5.5}WO_{11.25-\delta}$ (NWO) powder was synthetized by the citrate-complexation route modified to stabilize W- and Nd-containing ions following the methodology outlined in previous works [58, 59]. NWO powders were calcined at 900 ºC for 10 h to obtain the fluorite single phase. The selected stoichiometry is related to the fact that $La_{6-x}WO_{12-y}$ (with y = 1.5x + δ) based materials present only single phase within a narrow La/W range, ranging from 5.2 to 5.6 depending on the sintering temperature [41, 42, 60, 61]. Furthermore, $Nd_{5.5}WO_{11.25-\delta}$ has been reported to be mixed electronic-ionic conductor and stable under different atmospheres [23] similar as $La_{5.5}WO_{11.25-\delta}$ that presents good performance in terms of hydrogen permeation and stability [24, 62]

2.1. Mechanical characterization

The samples used in the mechanical characterization were prepared using the NWO powder previously calcined at 900 ° C and uniaxially pressed at 100 MPa. Subsequently, green bars were sintered in air at 1550 ° C for 5 h.

The room temperature elastic properties were determined with depth-sensitive indentation using a Vickers micro-indentation device HC100 (Helmut Fischer KG, Sindelfingen, Germany) on grinded and subsequently polished cross-section surface specimens (20×0.2 mm^2) according to guidelines outlined in ASTM C1327-08 [63]. The used indentation load was 1000 mN.

For creep tests, the sintered bars were machined to dimensions ~ $2.6 \times 3.2 \times 9.5$ mm^3. The (2.6×3.2 mm^2) end-faces of the samples were parallelized by grinding and finally polished for ~ 1 h using 1 μm diamond paste in order to minimize surface effects and superimposed bending by misalignments. Compressive creep tests were performed in ambient air under a constant uniaxial load, corresponding to nominal stresses in the range of 10 to 63 MPa, using an electromechanical testing machine (Instron 1362) equipped with a high temperature furnace. The samples were mounted between two alumina push rods. A linear variable differential transformer (LVDT, Sangami) was used for measuring the vertical displacement in a range ± 1 μm and with a precision of 1.25 μm. The load was controlled with a 10 kN

load cell (Interface 1210 ACK), while the temperature was monitored with a K-type thermocouple located near the sample surface. Creep measurements were conducted, in air, from 900 °C to 1350 °C. The temperature was incremented stepwise with 100 °C or 150 °C intervals, using heating rates of 0.5 °C /min. Additional details of the creep testing procedure are described elsewhere [64]. Below 1000 °C, no measureable creep deformation values were obtained and these measurements are not presented. Consequently, creep measurements were measured up to 1350 °C in order to have sufficient data to calculate accurately the activation energies and to reduce the uncertainty of the measurement.

Creep parameters were obtained by fitting the experimental data of the steady-state creep rate, $\dot{\varepsilon}$, to the generalized power law relationship [65]:

$$\dot{\varepsilon} = A \cdot \left(\frac{1}{d}\right)^p \cdot \sigma^n \cdot exp\left(-\frac{Q_a}{RT}\right) \tag{1}$$

where A is a proportionality parameter, d the grain size, p the inverse grain size exponent, σ the applied stress, n the stress exponent, Q_a the apparent activation energy, R the universal gas constant and T the temperature. The value for n, at a given temperature, was calculated from the slope of the log-log plot of $\dot{\varepsilon}$ versus σ (Norton plot). The value for Q_a, at a constant stress, was calculated from the slope of the $\dot{\varepsilon}$ - Arrhenius plot.

Microstructural analysis was performed using scanning electron microscopy (SEM, SUPRA 50VP and Merlin, both Zeiss, Germany) on samples polished with diamond paste down to 0.25 μm. Elemental analysis was carried out by energy-dispersive X-Ray spectroscopy (EDS, Inca, Oxford Inst.). For porosity analysis of sintered specimens, SEM images of cross-sections were recorded and analysed using the Analysis Pro® analysis software (Olympus).

2.2. Chemical stability

Pellets employed for the stability tests were manufactured by uniaxial pressing at 30 kN of powders previously calcined at 900 °C (mean crystallite size ~ 25 nm) [23]. Subsequently, pellets were sintered at 1550 °C for 10 h, obtaining a relative density of around 95%. Thickness of the specimen for electrochemical characterization was 530 μm.

NWO sample was exposed consecutively to different H_2S and H_2 concentrations (from lower to higher concentration) at 827 °C as illustrated in Figure 1. All the streams were saturated in water at room temperature (2.5 % H_2O). The four different conditions (obtained by the dilution of a cylinder composed of 1500 ppm H_2S in H_2 with N_2) on a dry basis are listed below.

T1: 330 ppm H_2S, 22% H_2 in N_2.
T2: 480 ppm H_2S, 32% H_2 in N_2.
T3: 705 ppm H_2S, 47% H_2 in N_2.

T4: 1500 ppm H_2S in H_2.

After each condition, the sample was cooled down under an atmosphere of N_2 saturated in water (2.5 % H_2O) in order to avoid the decomposition of any possible secondary phase formed during the treatment and subsequently it was analyzed by X-ray diffraction (XRD).
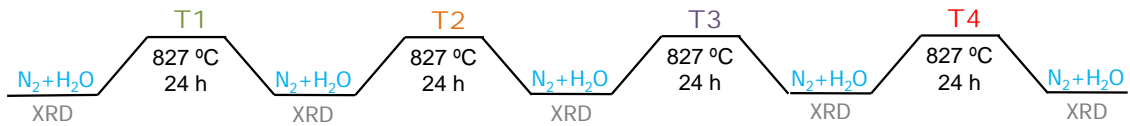

Figure 1: Scheme of the stability treatment.

Despite the reactions of interest will operate between 500-700 ºC, higher temperature was selected to evaluate the feasibility of the material under harder conditions than the operation ones. In fact, the temperature selection of these preliminary tests was based on the La-O-S phase stability diagram at 827 ºC that indicates the stability of the La_2O_2S phase [66] under the studied conditions shown in Figure 1.

XRD analysis was carried out on a PANalytical CubiX fast diffractometer using $CuK\alpha_{1,2}$ radiation and a X'Celerator detector in Bragg-Brentano geometry. XRD patterns were recorded in the 2θ range 20º to 70º and analysed using the software X'Pert Highscore Plus.

Electrochemical performance of the NWO was evaluated by means of electrochemical impedance spectroscopy (EIS) measurements. Measurements were performed in two-point four-wires configuration on disc-shaped samples using Pt as electrode. An EC-Lab SP-150 potentiostat equipped with a module for impedance analysis was employed for these measurements. Input signal was 0 V DC – 30 mV AC in the $0.02 – 5 \cdot 10^5$ Hz frequency range.

In order to study the influence of the H_2S on the NWO transport properties, EIS measurements were performed under a wet (2.5% H_2O) atmosphere composed of 10% H_2 and 1973 ppm of H_2S with balanced N_2 from 400 °C to 680 °C. The samples were annealed for 26 h at each temperature under these harsh conditions. After 26 h at 680 °C, the concentration of H_2S was increased to 4163 ppm and EIS measurements were performed for 26 h. This last concentration is typically found in the inlet of the water gas shift reactors in an integrated gasification combined cycle (IGCC) [35] process. The impedance of the material was previously measured under an atmosphere composed of wet 10% H_2 in N_2 (2.5% H_2O) from 680 °C to 400 ºC.

After these measurements, the sample was analyzed by XRD and SEM in order to study the microstructure and the possible formation of the secondary phases. Cell parameter refinements were performed using the X'Pert Highscore Plus software. SEM analysis was performed using a JEOL JXA-

8530F microprobe and a field-emission scanning electron microscope (FE-SEM) (Zeiss Ultra 55), equipped with WDS and EDX for elemental analysis, respectively.

3. Results and discussion

3.1. Mechanical properties

NWO samples used in the study of the mechanical properties were sintered at 1550 °C. Sintered material presents a cubic crystal structure (ICSD 189792), single phase fluorite, as it was checked by XRD. Microstructure of the materials was studied due to the important role that can play in the mechanical properties. SEM images of the polished cross-section and the thermally etched (at 1500 °C for 30 min) cross-section of the NWO samples are presented in Figure 2a and b, respectively. Dense specimens have an homogeneous microstructure with ~ 8 % porosity and rather small grains with average grain size of 1 ± 0.5 µm as it is seen in Figure 2b.
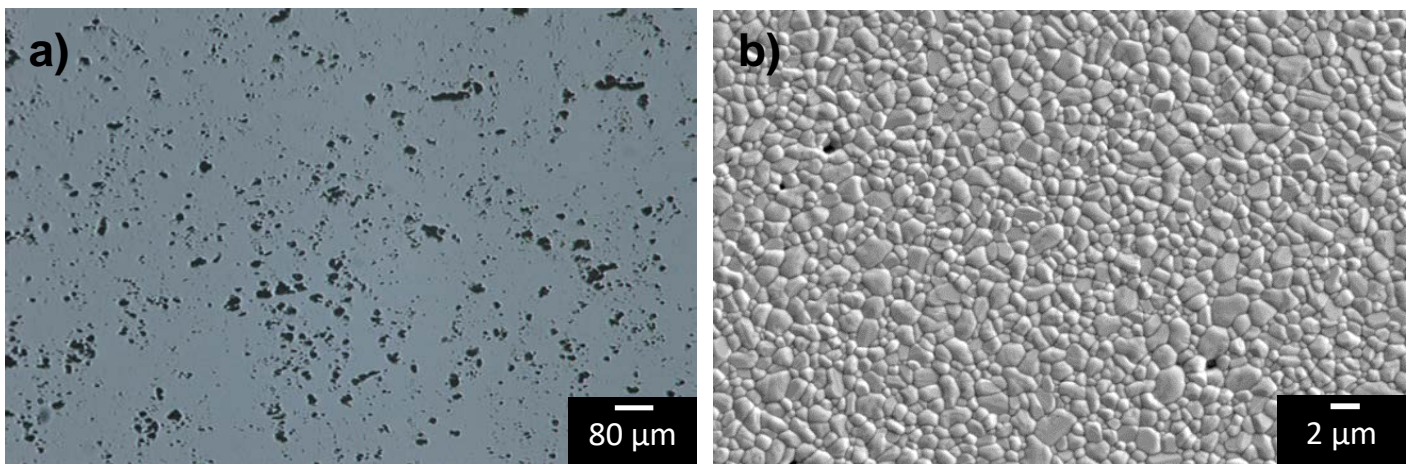

Figure 2: Microstructure of (a) polished cross-section and (b) thermally etched (1500 °C 30 min) cross-section of the NWO samples sintered at 1550 °C in air.

The room temperature elastic modulus determined by indentation testing was $E_{IT} = 125 \pm 5$ GPa. An average elastic modulus of ~ 120 GPa at room temperature was previously reported for LWO54 [52, 53], indicating the similar performance of both materials. The determined elastic modulus of NWO is lower than the reported for $BaZrO_3$ (240 GPa) [67] and $BaCeO_3$ (154 GPa) [68] and higher than the obtained for LaNbO4 (95 GPa)[69].

The obtained creep parameters (Eq. 1) are summarized in Table 1 (apparent activation energy Q_a) and Table 2 (Stress exponent n). Measurable deformation rates were obtained at $T \geq 1050$ °C for all stresses, which indicates that NWO is surely a suitable candidate membrane material at the relevant operation temperatures (600-800 °C).

The average stress exponent of n = 1.3 ± 0.2 along with an activation energy of Q_a = 540 ± 30 kJ/mol suggests a diffusional creep mechanism. The stress exponent increases above 1150 °C, indicating contributions of additional creep mechanisms. However, no significant change in activation energy is observed with increasing temperature. Diffusivity studies by Vøllestad et al. [70] verified that enhanced grain boundary diffusion takes place for cation migration of this compound, which could lead to slightly increased activation energy and/or stress exponent.

Table 1: Apparent activation energy (Q_a) at a given stress and different temperature ranges

Stress	Q_a (kJ/mol)	
	1050 – 1250 °C	1250 – 1350 °C
20	495 ± 45	580
40	525 ± 20	565
63	544	

Table 2: Stress exponent (n) at a given temperature

Temperature (°C)	n
1050	0.9 ± 0.03
1150	1.6 ± 0.03
1250	1.4
1350	1.3

Mechanical properties of LWO54 have been recently reported [52]. Creep studies for both materials, NWO and LWO54, indicate a diffusional creep mechanism. Overall, NWO exhibited higher creep rates in comparison to LWO54, but this effect is attributed to microstructural differences in the studied samples, i.e. smaller grain size and higher porosity.

The variation of Q_a and n with temperature is not as profound as in the case of LWO54 (Table 3). Moreover, Q_a for NWO is 544 kJ/mol, higher than the 210 kJ/mol obtained for LWO54 with a grain size of 11 μm, both at 63 MPa and 1050-1250 °C range. Note that the diffusion creep mechanism is controlled from the slowest species via the fastest diffusion path. The ionic radius of La^{3+} (1.1Å) is bigger than Nd^{3+} (1.046Å), both with a coordination number (c.n.) of 7 and also bigger than W^{6+} (c.n.=6) (0.6Å), which would not agree with the Q_a increase (see Table 3). The creep mechanism of LWO54 is controlled by combined diffusion of cations along the grain boundaries and/or lattice as it was deduced from the change of the Q_a at 1250 °C and the n, p parameters at the tested temperature and stress range. Consequently, it can be suggested that Nd cation controls the diffusion mechanism (up to 1350 °C and 63MPa) as the largest cation in the material. Regarding the diffusion path of the migrating cations, the small variation of the Q_a and the small grain size (~1μm) can indicate a Coble creep model, *i.e.*, the diffusion occurs along the grain boundaries.

In order to predict the long-term performance of a membrane structure, a maximum tolerable creep deformation has to be defined. According to Thomson et al. [71], membrane materials should not creep in a compressive mode more that 1 % per year in order to warrant reliable long term operation. On the other hand, Schulz et al. [72] calculated that the compressive stress exerted on an oxygen membrane during operation in a CO_2 operation system to be approximately 30 MPa, hence as a guideline for the analysis the creep should be less than 1 % / year for a stress of 30 MPa. The creep rates depend almost exponentially on temperature and thus can easily be extrapolated to the application relevant temperature range 600-800 °C, where they are lower than the 1 % strain per year limit [71]. Figure 3 compares the creep rates in air for a stress of 40 MPa for NWO and LWO54 as a function of temperature from 1050 °C to 1450 °C. In addition, Table 3 presents more information on the creep parameters for LWO and for other hydrogen transport membrane materials and possible substrate materials. In a previous study [52], creep rates under dry and wet 4% H_2 in Ar were measured for LWO54 and no significant effect of H_2 was observed, being the creep rate slightly lower than in air. Due to the complexity of the measurement and the expected similar behaviour to the LWO54, NWO was not measured under H_2-containing atmosphere.
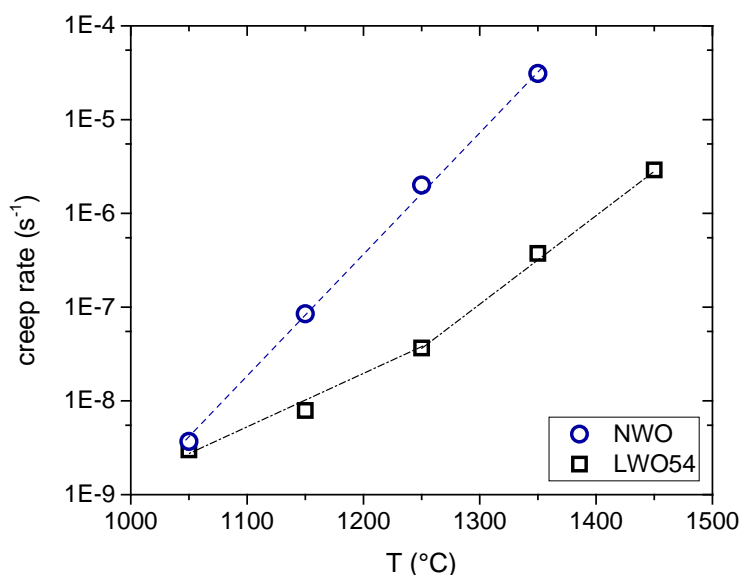

Figure 3 Creep rates in air as a function of the temperature for NWO and LWO54 for a stress of 40 MPa [52].

Table 3: Creep parameters for hydrogen transport membranes and possible substrate materials.

Material	Q_a	n	Mechanism	Testing conditions	Grain size (µm)	Ref
BaZrO₃	460±30	0.9±0.1	Diffusion/ GBS	1300-1400 °C 10-100 MPa	~4	[67]
BaCe₀.₉₈Y₀.₂O₃₋δ	343±30	1.1±0.1	Diffusion	1200-1450 °C 1-150 MPa	~9	[73]
CeO₂	160±60	2.3±1.1	Diffusion/	800-900 °C	16±6	[74]

			Dislocation	60-120 MPa		
LWO54	210±30 480	1.1±0.4	Diffusion	1050-1250°C 20-63 MPa 1250-1450°C 20-63 MPa	11 ± 4	[52]
MgO	385±15	4.3-4.9	Dislocation	800-1200 °C 30-100 MPa	15±10	[67]

3.2. Chemical stability under H₂S containing atmospheres

The chemical stability of NWO under H_2S containing atmospheres was evaluated. NWO pellets were exposed consecutively at different humidified H_2S- and H_2- containing atmospheres at 827 ºC: 330 ppm H_2S and 22% H_2 in N_2 (T1), 480 ppm H_2S and 32% H_2 in N_2 (T2), 705 ppm H_2S and 47% H_2 in N_2 (T3) and 1500 ppm H_2S balanced with H_2 (T4). All gas streams were saturated in water at room temperature (2.5 % H_2O). NWO samples were annealed under each atmosphere for 24h, then the sample was cooled down under an atmosphere of N_2 saturated with water in order to avoid the decomposition of possibly formed sulfides, and subsequently it was analyzed by XRD (Figure 4). A magnification of the XRD pattern area where the main diffraction peaks corresponding to Nd_2O_2S appear is shown in Figure 4b (note the *log* scale in y-axis). The formation of Nd_2O_2S or formation of secondary phases was not detected within the resolution limit of the XRD setup. Note that $BaCeO_3$ based material decomposed when it was exposed to an atmosphere composed of 115ppm H_2S, 4.43% CO_2, 2.12% CO and 92.09% H_2 at 500 ºC and 40 bar [18].
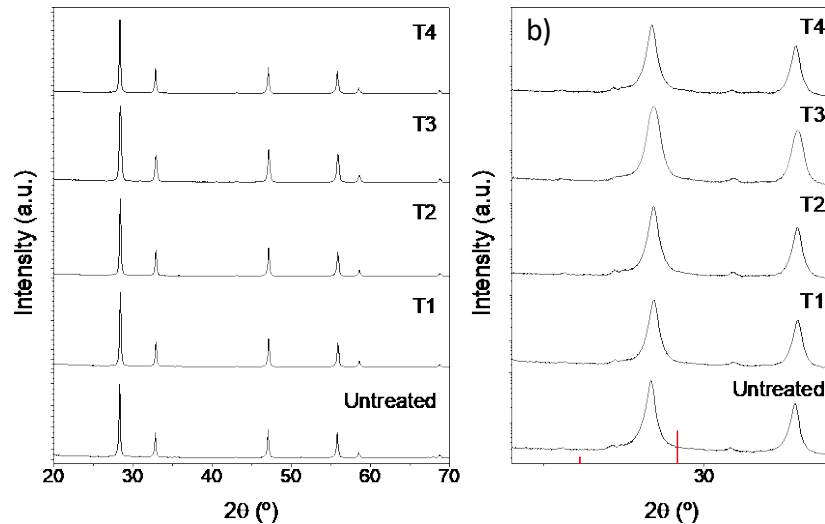

Figure 4: XRD patterns before and after the T1, T2, T3 and T4 treatments at 827 ºC from 20 to 70 º (a) and a magnification from 24 to 34° (y-axis in *log* scale). Main diffraction peaks corresponding to Nd_2O_2S have been marked in red (b).

The sample microstructure after the stability treatments was analyzed by FE-SEM. Micrographs of the cross-section fracture are shown in Figure 5. Formation of new phases in the bulk is not detected by the

10

SEM analysis, nevertheless changes in the morphology are observed. An important number of occluded pores present different morphology than the rest of the sample as can be observed in Figure 5b-d. The EDS analysis detected sulfur in these areas whereas it was not identified in the rest of the sample. The different morphology could be related to the formation of dislocations and/or stacking faults due to the presence of sulfur and/or the reduction of the material [56]. This kind of morphology was not observed for NWO after conductivity or permeation measurements in previous studies [23] thus the thermal shock is dismissed as the cause.

Figure 5: Cross section FE-SEM micrographs after the H_2S stability treatments with different magnification (a-d).

Despite the stability under H_2S in case of short-term treatments, the different morphology and the presence of sulfur species could affect the transport through the crystalline structure. This effect was further assessed by EIS measurements. First, EIS measurements were performed at intervals of 100 °C over the range of 680-400 °C in wet reducing conditions (2.5% H_2O). The corresponding Bode and Nyquist plots are shown in Figure S1. The impedance spectra were fitted by using the equivalent circuit (R1Q1)(R2Q2) (see inset of the Figure S1) that can be assigned as bulk and electrodes contributions, respectively. Subsequently, the total conductivity was calculated. Under these conditions, NWO presents an important n-type electronic conductivity as can be ascertained from the increase of the

conductivity with the decrease of the pO_2 plotted in Figure 6. The observed total conductivity is in agreement with previous results obtained by DC-conductivity measurements [25, 55].
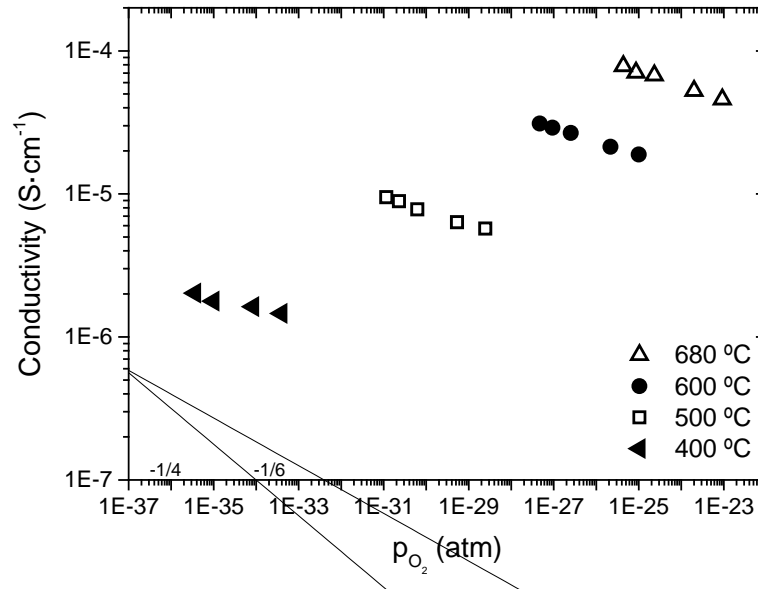

Figure 6: Total conductivity as a function of the pO_2 and temperature under wet reducing atmospheres.

Subsequently, H_2S was added to the gas stream, and the resulting atmosphere comprised wet 1973 ppm H_2S and 10% H_2 in N_2 balance (2.5% H_2). In this case, EIS measurements were performed from 400 °C to 680 °C for 26 h at each temperature. Nyquist and Bode plots obtained in these measurements are presented in the Supporting Information (Figure S2). Under these conditions, the contribution of the grain boundary resistance becomes important and the impedance spectra were fitted by using the equivalent circuit (R1Q1)(R2Q2)(R3Q3) corresponding to bulk, grain boundary and electrodes contributions, respectively.

Figure 7 shows the bulk and the grain boundary resistances (Figure 7a) and the total conductivity (Figure 7b) as a function of the temperature under wet 10% H_2 in N_2 atmospheres in presence of 0 ppm and 1973 ppm H_2S, respectively. Values under H_2S containing atmosphere were obtained after 26 h of exposition. At 400 °C, the total conductivity is slightly lower when H_2S is fed due to the important contribution of the grain boundary resistance that was negligible when no H_2S was fed as can be observed in Figure 7a. At 500 °C, the bulk resistance of the compound decreases but the grain boundary resistance is still important, giving rise to a similar total conductivity in both atmospheres. At higher temperature (600 and 700 °C), total conductivity increases due to the dominant drop of the bulk resistance, even though the grain boundary resistance has still some contribution. This is contrary to the behaviour reported for $BaZr_{0.85}Y_{0.15}O_3$ that presents lower conductivity (bulk and grain boundary) under 5000 ppm H_2S balanced with H_2 in the whole range of studied temperatures [36].

As can be observed in Figure 7b, conductivity follows an Arrhenius behavior and a change in the apparent activation energy occurs at 600 °C and 500 °C without and with H_2S in the feed, respectively. Activation energies differ depending on the atmosphere composition, i.e. they are higher when H_2S is fed. This fact could be related to the important contribution of the grain boundary resistance and the corresponding activation energy under H_2S atmospheres (see Figure 7a).

The total conductivity as a function of H_2S feeding time is plotted in Figure 7c. Stabilization of the conductivity takes some time depending on the temperature and then remains stable, indicating the stability of the equilibrated material. Regarding the electrodes, the resistance increases slightly when H_2S is fed. This effect is more important at 400 °C and 700 ºC, whereas at 500 °C and 600 ºC it is not significant.
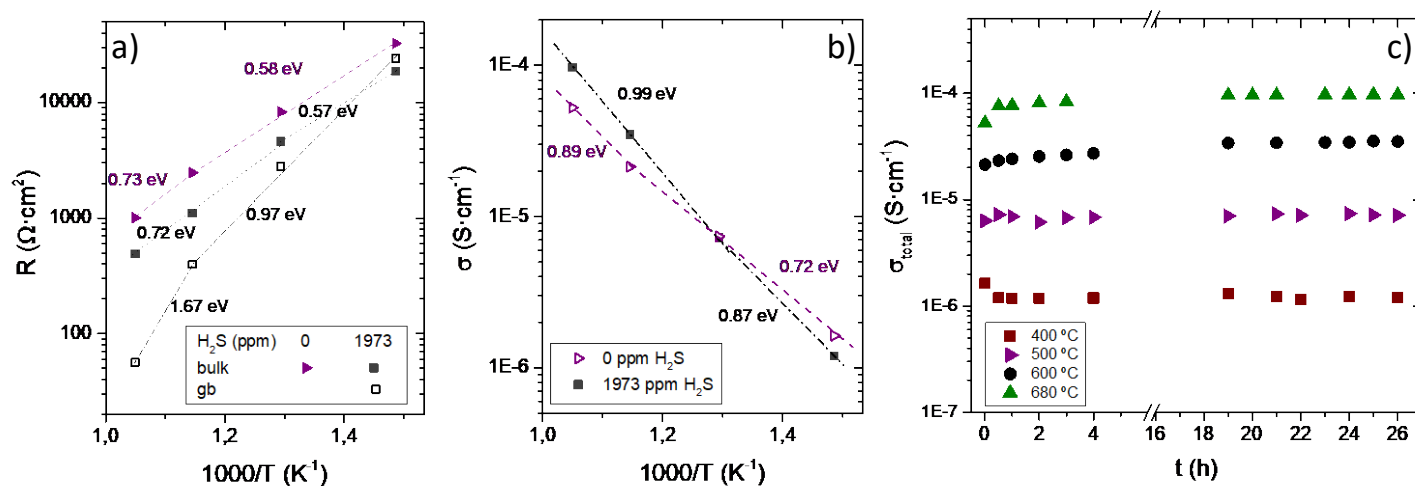

Figure 7: Electrochemical characterization in H_2S operation: (a) bulk and grain boundary resistance as a function of reciprocal temperature; (b) total conductivity as a function of reciprocal temperature after annealing for 26 hours; and (c) total conductivity as a function of time on stream and temperature. Gas atmosphere composed of wet 1973 ppm H_2S and 10% H_2 in N_2.

EIS measurements were subsequently carried out at 680 °C under a wet atmosphere composed of 4163 ppm H_2S and 10% H_2 in N_2 for 26 hours. The resulting total conductivity is plotted in Figure 8a as a function of time. Conductivity values remained stable throughout the course of the treatment in H_2S, even at this high H_2S concentration. Note that the same pellet was used in all the impedance measurements. Both, bulk and grain boundary resistances decrease when 4163 ppm H_2S is fed as compared with the measurements feeding 1973 ppm H_2S, especially the grain boundary resistance that decreases by approximately 40%.

After the EIS measurements, the sample was analyzed by SEM and XRD. SEM micrographs near the surface (b) and in the bulk (e) are shown in Figure 9. No secondary phases are observed in the BSE images (Figure 9a and d). WDS analysis (Figure 9c) indicates the presence of sulfur in the Pt layer, and an important concentration can be detected along the surface and in the pores near the surface. In the

13

bulk (Figure 9f), small quantities of sulfur are also detected, but the highest accumulation is located, as it was previously observed, within occluded pores.
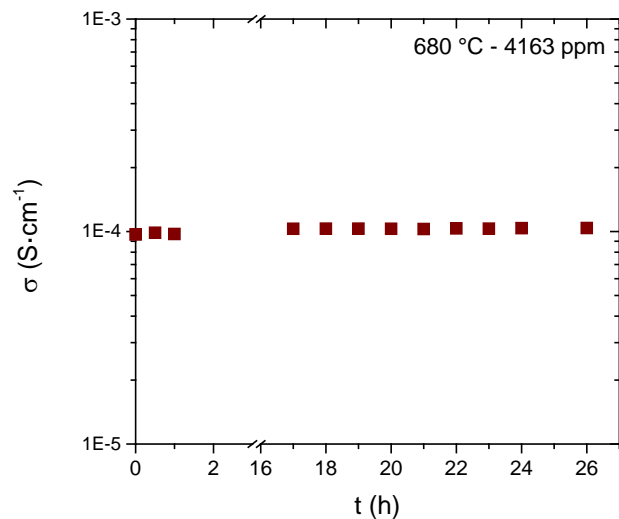

Figure 8: Total conductivity as a function of time when NWO is exposed to a wet atmosphere composed of 4163 ppm H_2S and 10% H_2 in N_2 for 26 h.
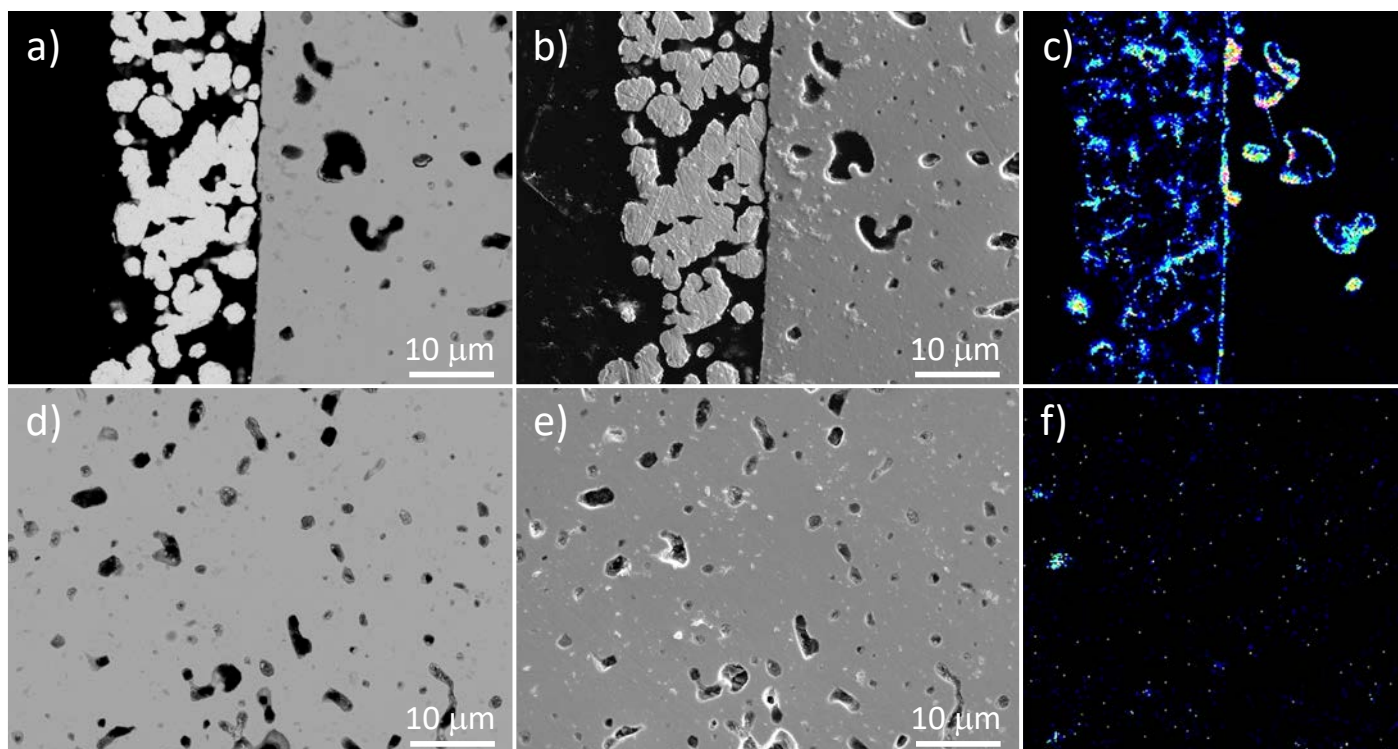

Figure 9: BSE (a,d) and SE (b,e) images and WDS map for sulfur (c,f) after the EIS measurements.

14

Figure 10 shows the SEM micrographs and the corresponding WDS maps for the different elements comprised in the electrode-membrane assembly. A S-rich area is observed on the surface of the material (pink color indicates higher concentration than blue color). The area where higher sulfur concentration is found overlaps with a W-poor region. The O concentration in this area is lower than in the rest of the material. The WDS analysis in this region (pointed as 1) indicates the predominant presence of Nd_2O_2S. However, the analysis in the area pointed as 2, also rich in S, indicates that the average stoichiometry of the compound is $Nd_{5.8}WO_{10.05}$ with minor presence of S. This sulfur could be incorporated in the crystalline structure of the NWO as no secondary phases are found. The analysis in region 3 matches with that in region 2. It should be pointed out that Nd_2O_2S was only detected on the surface, no evidence for this phase was detected in the bulk.
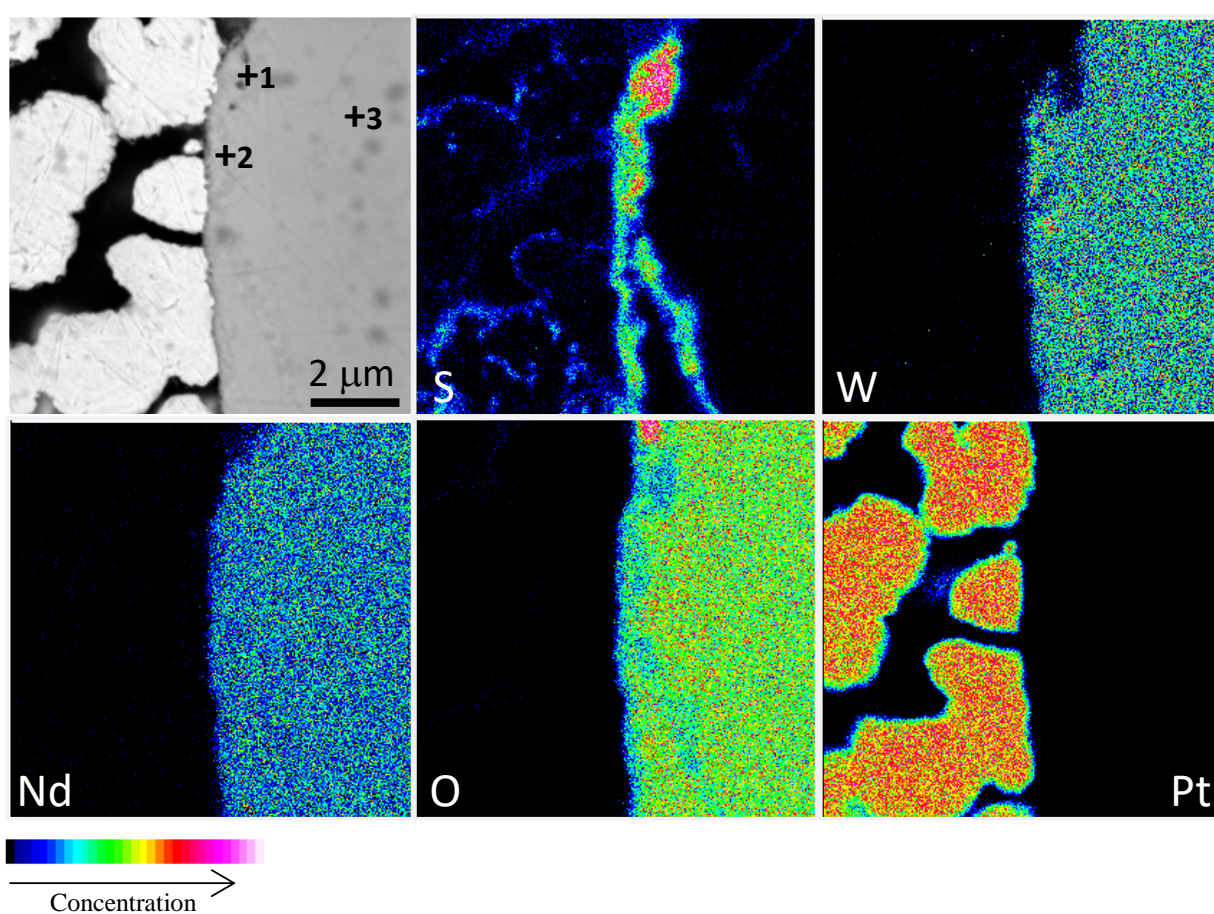

Figure 10: BSE image and WDS map for S, W, Nd, O and Pt after the EIS measurements.

The NWO sample was further characterized by FE-SEM and XRD. Figure 11a, b and c shows the micrographs of the surface and the area near the surface and a magnification of some of the occluded pores found in this area, respectively. The same morphology was found in the occluded pores than in the previous treated sample (see Figure 5). Furthermore, sulfur was only detected in these dislocations and the extension of them is lower in the bulk of the membrane. The formation of these dislocations might be responsible for the increase of the grain boundary resistance.

XRD reveals some secondary products in the surface that could be indexed as Nd_2O_3 and Nd_2O_2S (Figure 11e) and are in agreement with WDS analysis near the surface. The origin of the formation of Nd_2O_2S as secondary phase can be the presence of minor Nd_2O_3 impurities in the as-sintered sample (Figure 11d). Cell parameters and cell volume before and after the EIS measurements were calculated. NWO presents cubic fluorite structure regardless the atmosphere exposition and the cell parameter increases from 5.455(1) to 5.4596 (6) Å after the H_2S treatment. Consequently, the volume cell increases from 162.36 to 162.74 Å^3.
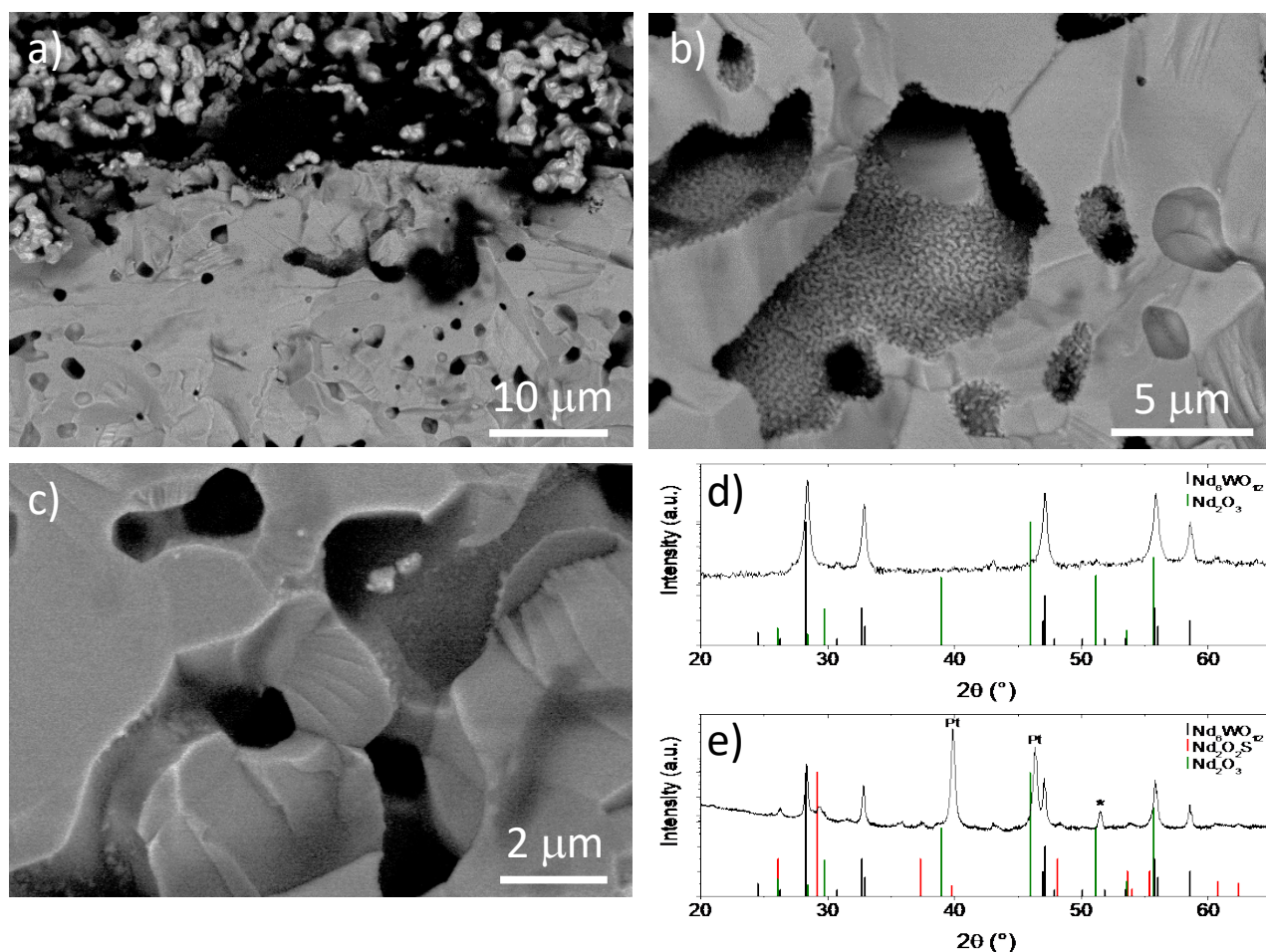

Figure 11: FE-SEM micrographs near the surface (a,b) and in the bulk (c) and XRD of the sample before (d) and after (e) the EIS measurements (* corresponds to sample holder).

From these results, some sulfur incorporation in the NWO structure can be hypothesized and the increase of the total conductivity at high temperature (T>600 °C) could be explained by different hypotheses. First, the incorporation of S^{2-} in the structure could produce an increase in the electronic conductivity, the protonic conductivity of the material or transport of S^{2-} ions through the structure. If S^{2-} transport through the material is considered, a higher activation energy should be expected due to the higher size of the sulfide-ion relative to the oxide-ion [75], and this fact would explain the activation energy increase observed in Figure 7. On the other hand, proton transport in $SrZrS_3$ and $BaZrS_3$ has been found to be comparable or more favorable than in the $SrZrO_3$ oxide [76]. In this case, one could speculate that proton

16

transport has been improved by the incorporation of S^{2-}. In contrast, this conductivity increase could be due to the so-called *sulfur enhancement* in fuel cells that describes the improvement of the fuel cell performance due to the decrease of the interfacial resistance in the anodes at high temperature and high concentration of H_2S due to the formation of a very thin layer of conductive sulfides on the oxide surface [77]. By XRD we found traces of Nd_2O_2S, and a thin layer rich in sulfur was detected by WDS (see Figure 9 and Figure 10). To the best of our knowledge, no conductivity data for Nd_2O_2S in this range of temperature (600-700 °C) has been reported.

Despite the improvement of the conductivity under H_2S-containing atmospheres and the stability of the compound, more sophisticated structural and transport characterization are needed to discern the actual sulfur incorporation in the structure and the implications on the mixed electronic-protonic conduction.

4. Conclusions

$Nd_{5.5}WO_{11.25-\delta}$ is a suitable candidate membrane material regarding its mechanical properties as suggested by characterization results from micro-indentation at room temperature and creep measurements in air from 900 °C to 1350 °C. Measurable deformation rates were only obtained at $T \geq$ 1050 °C, and the creep rates were lower than 1 % strain per year in the operation temperature range 600-800 °C.

Stability under H_2S atmospheres was verified by XRD, SEM and EIS measurements. Total conductivity of the material was stable under all used atmospheres, even if containing 4163 ppm H_2S. Furthermore, an increase in the total conductivity at 600 °C and 700 °C was observed. SEM and WDS analysis confirm the presence of sulfur in the bulk of the material, mainly located in the occluded pores of the material. Nd_2O_2S was detected on the sample surface while the formation of this compound may be ascribed to minor traces of Nd_2O_3 already existing in the as-sintered material. The increase in the total conductivity might be assigned to the incorporation and transport of S^{2-} ions or the improvement of the protonic or electronic conductivity when S^{2-} is partially incorporated in the O^{2-} sublattice of NWO. However, so far not enough experimental evidences exist to determine the specific effect of the sulfur on NWO transport properties.

References

[1] Y.-M. Lin, S.-L. Liu, C.-H. Chuang, Y.-T. Chu, Effect of incipient removal of hydrogen through palladium membrane on the conversion of methane steam reforming: Experimental and modeling, Catalysis Today 82(1–4) (2003) 127-139.

[2] C.S. Patil, M. van Sint Annaland, J.A.M. Kuipers, Fluidised bed membrane reactor for ultrapure hydrogen production via methane steam reforming: Experimental demonstration and model validation, Chemical Engineering Science 62(11) (2007) 2989-3007.

[3] L. Barelli, G. Bidini, F. Gallorini, S. Servili, Hydrogen production through sorption-enhanced steam methane reforming and membrane technology: A review, Energy 33(4) (2008) 554-570.

[4] T. Boeltken, A. Wunsch, T. Gietzelt, P. Pfeifer, R. Dittmeyer, Ultra-compact microstructured methane steam reformer with integrated Palladium membrane for on-site production of pure hydrogen: Experimental demonstration, International Journal of Hydrogen Energy 39(31) (2014) 18058-18068.

[5] S.H. Morejudo, R. Zanón, S. Escolástico, I. Yuste-Tirados, H. Malerød-Fjeld, P.K. Vestre, W.G. Coors, A. Martínez, T. Norby, J.M. Serra, C. Kjølseth, Direct conversion of methane to aromatics in a catalytic co-ionic membrane reactor, Science 353(6299) (2016) 563-566.

[6] G. Saracco, H.W.J.P. Neomagus, G.F. Versteeg, W.P.M.v. Swaaij, High-temperature membrane reactors: potential and problems, Chemical Engineering Science 54(13–14) (1999) 1997-2017.

[7] X. Dong, W. Jin, N. Xu, K. Li, Dense ceramic catalytic membranes and membrane reactors for energy and environmental applications, Chemical Communications 47(39) (2011) 10886-10902.

[8] B. Dittmar, A. Behrens, N. Schödel, M. Rüttinger, T. Franco, G. Straczewski, R. Dittmeyer, Methane steam reforming operation and thermal stability of new porous metal supported tubular palladium composite membranes, International Journal of Hydrogen Energy 38(21) (2013) 8759-8771.

[9] K. Jordal, R. Bredesen, H.M. Kvamsdal, O. Bolland, Integration of H_2-separating membrane technology in gas turbine processes for CO_2 capture, Energy 29(9-10) (2004) 1269-1278.

[10] J.W. Phair, S.P.S. Badwal, Review of proton conductors for hydrogen separation, Ionics 12(2) (2006) 103-115.

[11] H. Iwahara, Technological challenges in the application of proton conducting ceramics, Solid State Ionics 77 (1995) 289-298.

[12] K.D. Kreuer, PROTON-CONDUCTING OXIDES, Annual Review of Materials Research 33(1) (2003) 333-359.

[13] K.H. Ryu, S.M. Haile, Chemical stability and proton conductivity of doped $BaCeO_3$–$BaZrO_3$ solid solutions, Solid State Ionics 125(1–4) (1999) 355-367.

[14] W. Münch, K.D. Kreuer, G. Seifert, J. Maier, Proton diffusion in perovskites: comparison between $BaCeO_3$, $BaZrO_3$, $SrTiO_3$, and $CaTiO_3$ using quantum molecular dynamics, Solid State Ionics 136–137 (2000) 183-189.

[15] J. Song, L. Li, X. Tan, K. Li, $BaCe_{0.85}Tb_{0.05}Co_{0.1}O_{3-\delta}$ perovskite hollow fibre membranes for hydrogen/oxygen permeation, International Journal of Hydrogen Energy 38(19) (2013) 7904-7912.

[16] S.J. Song, E.D. Wachsman, J. Rhodes, H.S. Yoon, K.H. Lee, G. Zhang, S.E. Dorris, U. Balachandran, Hydrogen permeability and effect of microstructure on mixed protonic-electronic conducting Eu-doped strontium cerate, J Mater Sci 40(15) (2005) 4061-4066.

[17] Y. Wei, J. Xue, W. Fang, Y. Chen, H. Wang, J. Caro, Enhanced stability of Zr-doped Ba(CeTb)O$_{3-\delta}$-Ni cermet membrane for hydrogen separation, Chemical Communications 51(58) (2015) 11619-11621.

[18] S. Escolástico, M. Ivanova, C. Solís, S. Roitsch, W.A. Meulenberg, J.M. Serra, Improvement of transport properties and hydrogen permeation of chemically-stable proton-conducting oxides based on the system BaZr$_{1-x-y}$Y$_x$M$_y$O$_{3-\delta}$, RSC Advances 2(11) (2012) 4932-4943.

[19] J. Kniep, Y.S. Lin, Effect of Zirconium Doping on Hydrogen Permeation through Strontium Cerate Membranes, Industrial & Engineering Chemistry Research 49(6) (2010) 2768-2774.

[20] Z. Li, C. Kjølseth, R. Haugsrud, Hydrogen permeation, water splitting and hydration kinetics in Nd$_{5.4}$Mo$_{0.3}$W$_{0.7}$O$_{12-\delta}$, Journal of Membrane Science 476 (2015) 105-111.

[21] T. Oh, H. Yoon, J. Li, E.D. Wachsman, Hydrogen permeation through thin supported SrZr$_{0.2}$Ce$_{0.8-x}$Eu$_x$O$_{3-\delta}$ membranes, Journal of Membrane Science 345(1-2) (2009) 1-4.

[22] S. Ricote, N. Bonanos, G. Caboche, Water vapour solubility and conductivity study of the proton conductor BaCe(0.9 - x)ZrxY0.1O(3 - δ), Solid State Ionics 180(14-16) (2009) 990-997.

[23] S. Escolástico, M. Schroeder, J.M. Serra, Optimization of the mixed protonic-electronic conducting materials based on (Nd$_{5/6}$Ln$_{1/6}$)$_{5.5}$WO$_{11.25-\delta}$, Journal of Materials Chemistry A 2(18) (2014) 6616-6630.

[24] S. Escolástico, J. Seeger, S. Roitsch, M. Ivanova, W.A. Meulenberg, J.M. Serra, Enhanced H$_2$ separation through mixed proton-electron conducting membranes based on La$_{5.5}$W$_{0.8}$M$_{0.2}$O$_{11.25-\delta}$, ChemSusChem 6(8) (2013) 1523-32.

[25] S. Escolástico, S. Somacescu, J.M. Serra, Tailoring mixed ionic-electronic conduction in H$_2$ permeable membranes based on the system Nd$_{5.5}$W$_{1-x}$Mo$_x$O$_{11.25-\delta}$, Journal of Materials Chemistry A 3(2) (2015) 719-731.

[26] S. Escolástico, C. Solis, C. Kjolseth, J.M. Serra, Outstanding hydrogen permeation through CO$_2$-stable dual-phase ceramic membranes, Energy & Environmental Science 7(11) (2014) 3736-3746.

[27] E. Rebollo, C. Mortalo, S. Escolástico, S. Boldrini, S. Barison, J.M. Serra, M. Fabrizio, Exceptional hydrogen permeation of all-ceramic composite robust membranes based on BaCe$_{0.65}$Zr$_{0.20}$Y$_{0.15}$O$_{3-\delta}$ and Y- or Gd-doped ceria, Energy & Environmental Science 8(12) (2015) 3675-3686.

[28] W.A. Rosensteel, S. Ricote, N.P. Sullivan, Hydrogen permeation through dense BaCe$_{0.8}$Y$_{0.2}$O$_{3-\delta}$ - Ce$_{0.8}$Y$_{0.2}$O$_{2-\delta}$ composite-ceramic hydrogen separation membranes, International Journal of Hydrogen Energy 41(4) (2016) 2598-2606.

[29] M.E. Ivanova, S. Escolástico, M. Balaguer, J. Palisaitis, Y.J. Sohn, W.A. Meulenberg, O. Guillon, J. Mayer, J.M. Serra, Hydrogen separation through tailored dual phase membranes with nominal composition BaCe$_{0.8}$Eu$_{0.2}$O$_{3-\delta}$:Ce$_{0.8}$Y$_{0.2}$O$_{2-\delta}$ at intermediate temperatures, Scientific Reports 6 (2016).

[30] J. Li, H. Yoon, T.-K. Oh, E.D. Wachsman, High temperature SrCe$_{0.9}$Eu$_{0.1}$O$_{3-\delta}$ proton conducting membrane reactor for H$_2$ production using the water–gas shift reaction, Applied Catalysis B: Environmental 92(3–4) (2009) 234-239.

[31] J. Li, H. Yoon, T.-K. Oh, E.D. Wachsman, SrCe$_{0.7}$Zr$_{0.2}$Eu$_{0.1}$O$_3$-based hydrogen transport water gas shift reactor, International Journal of Hydrogen Energy 37(21) (2012) 16006-16012.

[32] V. Kyriakou, I. Garagounis, A. Vourros, E. Vasileiou, A. Manerbino, W.G. Coors, M. Stoukides, Methane steam reforming at low temperatures in a BaZr$_{0.7}$Ce$_{0.2}$Y$_{0.1}$O$_{2.9}$

proton conducting membrane reactor, Applied Catalysis B: Environmental 186 (2016) 1-9.

[33] J. Xue, Y. Chen, Y. Wei, A. Feldhoff, H. Wang, J. Caro, Gas to Liquids: Natural Gas Conversion to Aromatic Fuels and Chemicals in a Hydrogen-Permeable Ceramic Hollow Fiber Membrane Reactor, ACS Catalysis (2016) 2448-2451.

[34] Z. Liu, L. Li, E. Iglesia, Catalytic Pyrolysis of Methane on Mo/H-ZSM5 with Continuous Hydrogen Removal by Permeation Through Dense Oxide Films, Catalysis Letters 82(3) 175-180.

[35] B. Morreale, J. Ciferno, B. Howard, M. Ciocco, J. Marano, O. Iyoha, R. Enick, Gasification and associated degradation mechanisms applicable to dense metal hydrogen membranes, Inorganic Membranes for Energy and Environmental Applications2009, pp. 173-201.

[36] J. Li, J.-L. Luo, K.T. Chuang, A.R. Sanger, Chemical stability of Y-doped Ba(Ce,Zr)O3 perovskites in H2S-containing H2, Electrochimica Acta 53(10) (2008) 3701-3707.

[37] D. Medvedev, J. Lyagaeva, S. Plaksin, A. Demin, P. Tsiakaras, Sulfur and carbon tolerance of BaCeO3–BaZrO3 proton-conducting materials, Journal of Power Sources 273 (2015) 716-723.

[38] T. Kraia, S. Wachowski, E. Vøllestad, R. Strandbakke, M. Konsolakis, T. Norby, G.E. Marnellos, Electrochemical performance of Co_3O_4/CeO_2 electrodes in H_2S/H_2O atmospheres in a proton-conducting ceramic symmetrical cell with $BaZr_{0.7}Ce_{0.2}Y_{0.1}O_3$ solid electrolyte, Solid State Ionics 306 (2017) 31-37.

[39] E. Forster, D. van Holt, M.E. Ivanova, S. Baumann, W.A. Meulenberg, M. Müller, Stability of ceramic materials for H2 transport membranes in gasification environment under the influence of gas contaminants, Journal of the European Ceramic Society 36(14) (2016) 3457-3464.

[40] W. Deibert, F. Schulze-Küppers, E. Forster, M.E. Ivanova, M. Müller, W.A. Meulenberg, Stability and sintering of MgO as a substrate material for Lanthanum Tungstate membranes, Journal of the European Ceramic Society 37(2) (2017) 671-677.

[41] J. Seeger, M.E. Ivanova, W.A. Meulenberg, D. Sebold, D. Stover, T. Scherb, G. Schumacher, S. Escolástico, C. Solís, J.M. Serra, Synthesis and Characterization of Nonsubstituted and Substituted Proton-Conducting $La_{6-x}WO_{12-y}$, Inorganic Chemistry 52(18) (2013) 10375-10386.

[42] A. Magrasó, C. Frontera, D. Marrero-López, P. Núñez, New crystal structure and characterization of lanthanum tungstate "La_6WO_{12}" prepared by freeze-drying synthesis, Dalton Transactions (46) (2009) 10273-10283.

[43] M. Flytzani-Stephanopoulos, M. Sakbodin, Z. Wang, Regenerative Adsorption and Removal of H2S from Hot Fuel Gas Streams by Rare Earth Oxides, Science 312(5779) (2006) 1508.

[44] Z. Wang, M. Flytzani-Stephanopoulos, Cerium Oxide-Based Sorbents for Regenerative Hot Reformate Gas Desulfurization, Energy & Fuels 19(5) (2005) 2089-2097.

[45] K. Svoboda, J. Leitner, J. Havlica, M. Hartman, M. Pohořelý, J. Brynda, M. Šyc, Y.-P. Chyou, P.-C. Chen, Thermodynamic aspects of gasification derived syngas desulfurization, removal of hydrogen halides and regeneration of spent sorbents based on $La_2O_3/La_2O_2CO_3$ and cerium oxides, Fuel 197(Supplement C) (2017) 277-289.

[46] G. Pećanac, S. Baumann, J. Malzbender, Mechanical properties and lifetime predictions for $Ba_{0.5}Sr_{0.5}Co_{0.8}Fe_{0.2}O_{3-\delta}$ membrane material, Journal of Membrane Science 385-386(1) (2011) 263-268.

[47] B.X. Huang, J. Malzbender, R.W. Steinbrech, P. Grychtol, C.M. Schneider, L. Singheiser, Anomalies in the thermomechanical behavior of $Ba_{0.5}Sr_{0.5}Co_{0.8}Fe_{0.2}O_{3-\delta}$ ceramic oxygen conductive membranes at intermediate temperatures, Applied Physics Letters 95(5) (2009).

[48] B. Huang, J. Malzbender, R.W. Steinbrech, Elastic anomaly and internal friction of $Ba_{0.5}Sr_{0.5}Co_{0.8}Fe_{0.2}O_{3-\alpha}$ and $La_{0.58}Sr_{0.4}Co_{0.2}Fe_{0.8}O_{3-\alpha}$, Journal of Materials Research 26(11) (2011) 1388-1391.

[49] B.X. Huang, J. Malzbender, R.W. Steinbrech, L. Singheiser, Mechanical properties of $La_{0.58}Sr_{0.4}Co_{0.2}Fe_{0.8}O_{3-\delta}$ membranes, Solid State Ionics 180(2-3) (2009) 241-245.

[50] W. Araki, Y. Arai, J. Malzbender, Transitions of $Ba_{0.5}Sr_{0.5}Co_{0.8}Fe_{0.2}O_{3-\delta}$ and $La_{0.58}Sr_{0.4}Co_{0.2}Fe_{0.8}O_{3-\delta}$, Materials Letters 132 (2014) 295-297.

[51] W. Araki, J. Malzbender, Ferroelastic deformation of $La_{0.58}Sr_{0.4}Co_{0.2}Fe_{0.8}O_{3-\delta}$ under uniaxial compressive loading, Journal of the European Ceramic Society 33(4) (2013) 805-812.

[52] V. Stournari, Thermo-mechanical properties of Mixed Ionic-Electronic Conducting Membranes for Gas Separation, 2016.

[53] J.J. Roa, A. Magrasó, M. Morales, P. Núñez, M. Segarra, Determination of hardness, Young's modulus and fracture toughness of lanthanum tungstates as novel proton conductors, Ceramics International 37(5) (2011) 1593-1599.

[54] V. Stournari, W. Deibert, M.E. Ivanova, C. Krautgasser, R. Bermejo, J. Malzbender, Mechanical properties of tape casted Lanthanum Tungstate for membrane substrate application, Ceramics International 42(14) (2016) 15177-15182.

[55] S. Escolástico, J.M. Serra, $Nd_{5.5}W_{1-x}U_xO_{11.25-\delta}$ system: Electrochemical characterization and hydrogen permeation study, Journal of Membrane Science 489 (2015) 112-118.

[56] S. Escolástico, S. Somacescu, J.M. Serra, Solid State Transport and Hydrogen Permeation in the System $Nd_{5.5}W_{1-x}Re_xO_{11.25-\delta}$, Chemistry of Materials 26(2) (2014) 982-992.

[57] H. Liu, Y. Chen, Y. Wei, H. Wang, CO2-tolerant U-shaped hollow fiber membranes for hydrogen separation, International Journal of Hydrogen Energy (2016).

[58] S. Escolástico, C. Solís, J.M. Serra, Hydrogen separation and stability study of ceramic membranes based on the system Nd_5LnWO_{12}, International Journal of Hydrogen Energy 36(18) (2011) 11946-11954.

[59] S. Escolástico, V.B. Vert, J.M. Serra, Preparation and Characterization of Nanocrystalline Mixed Proton-Electronic Conducting Materials Based on the System Ln_6WO_{12}, Chemistry of Materials 21(14) (2009) 3079-3089.

[60] A. Magrasó, R. Haugsrud, Effects of the La/W ratio and doping on the structure, defect structure, stability and functional properties of proton-conducting lanthanum tungstate $La_{28-x}W_{4+x}O_{54+\delta}$. A review, Journal of Materials Chemistry A 2(32) (2014) 12630-12641.

[61] T. Scherb, S.A.J. Kimber, C. Stephan, P.F. Henry, G. Schumacher, S. Escolástico, J.M. Serra, J. Seeger, J. Just, A.H. Hill, J. Banhart, Nanoscale order in the frustrated mixed conductor $La_{5.6}WO_{12-\delta}$, Journal of Applied Crystallography 49 (2016) 997-1008.

[62] S. Escolástico, C. Solís, T. Scherb, G. Schumacher, J.M. Serra, Hydrogen separation in $La_{5.5}WO_{11.25-\delta}$ membranes, Journal of Membrane Science 444 (2013) 276-284.

[63] A. ASTM C1327-08 Standard Test Method for Vickers Indentation Hardness of Advanced Ceramics, West Conshohocken, PA, 2008.

[64] S.F.P. ten Donkelaar, V. Stournari, J. Malzbender, A. Nijmeijer, H.J.M. Bouwmeester, High-temperature compressive creep behaviour of perovskite-type oxides $SrTi_{1-x}Fe_xO_{3-\delta}$, Journal of the European Ceramic Society 35(15) (2015) 4203-4209.

[65] D.J. Green, An Introduction to the Mechanical Properties of Ceramics, in: C.S.S.S. Series (Ed.) Cambridge University Press, 1998.

[66] D.A.R. Kay, S.V. Subramanian, V. Kumar, V. Meng, R.K. Dwivedi, The use of RE_2O_2S phase stability diagrams in gaseous desulfurisation and iron and steel production, Inorg Chim Acta 94(1) (1984) 132-134.

[67] K.C. Goretta, E.T. Park, R.E. Koritala, M.M. Cuber, E.A. Pascual, N. Chen, A.R. De Arellano-Löpez, J.L. Routbort, Thermomechanical response of polycrystalline $BaZrO_3$, Physica C: Superconductivity and its Applications 309(3-4) (1998) 245-250.

[68] S. Yamanaka, M. Fujikane, T. Hamaguchi, H. Muta, T. Oyama, T. Matsuda, S.I. Kobayashi, K. Kurosaki, Thermophysical properties of $BaZrO_3$ and $BaCeO_3$, Journal of Alloys and Compounds 359(1-2) (2003) 109-113.

[69] T. Takagi, Y.H. Choa, T. Sekino, K. Niihara, Fabrication and Mechanical Properties of LaNbO4 and LaNbO4/Al2O3 Composites, Key Engineering Materials, 1999, pp. 181-184.

[70] E. Vøllestad, T. Norby, R. Haugsrud, Inter-diffusion in lanthanum tungsten oxide, Solid State Ionics 244 (2013) 57-62.

[71] D.R. Thomson, L.E. Bool, J.C. Chen, Oxygen enhanced combustion for NOx control, Praxair, 2004.

[72] M. Schulz, R. Kriegel, W. Burckhardt, Modeling of oxygen flux and stress distribution for $Ba_{0.5}Sr_{0.5}Co_{0.8}Fe_{0.2}O_{3-\delta}$ membranes at application conditions, 10th International Conference of Inorganic Membranes, Japan, 2008.

[73] K.C. Goretta, E.T. Park, J. Guan, U. Balachandran, S.E. Dorris, J.L. Routbort, Diffusional creep of $BaCe_{0.8}Y_{0.2}O_{3-\alpha}$ mixed conductors, Solid State Ionics 111(3-4) (1998) 295-299.

[74] M. Lipińska-Chwałek, G. Pećanac, J. Malzbender, Creep behaviour of membrane and substrate materials for oxygen separation units, Journal of the European Ceramic Society 33(10) (2013) 1841-1848.

[75] V.S. Johnson, K. Hellgardt, S.E. Dann, R.J. White, Synthesis and characterisation of a potential ceramic sulfide ion conductor based on the solid solution $xCaS:Nd_2S_3$, x = 0.7-1.0, J Mater Sci 42(6) (2007) 1948-1954.

[76] J.M. Polfus, T. Norby, R. Bredesen, Protons in oxysulfides, oxysulfates, and sulfides: A first-principles study of La_2O_2S, $La_2O_2SO_4$, $SrZrS_3$, and $BaZrS_3$, Journal of Physical Chemistry C 119(42) (2015) 23875-23882.

[77] Z. Cheng, J.-H. Wang, Y. Choi, L. Yang, M.C. Lin, M. Liu, From Ni-YSZ to sulfur-tolerant anode materials for SOFCs: electrochemical behavior, in situ characterization, modeling, and future perspectives, Energy & Environmental Science 4(11) (2011) 4380-4409.